# Illumination and communication conditions at the Mons Rümker region based on the improved Lunar Orbiter Laser Altimeter data

Jianguo Yan, Shanhong Liu, Xuan Yang, Chi Xiao, Mao Ye, Jin Weitong, Fei Li, Jean-Pierre Barriot

▶ **To cite this version:**

Jianguo Yan, Shanhong Liu, Xuan Yang, Chi Xiao, Mao Ye, et al.. Illumination and communication conditions at the Mons Rümker region based on the improved Lunar Orbiter Laser Altimeter data. Planetary and Space Science, 2019, 168, pp.73-82. 10.1016/j.pss.2019.01.010 . hal-03155650

**HAL Id: hal-03155650**
**https://upf.hal.science/hal-03155650**

Submitted on 2 Mar 2021

**HAL** is a multi-disciplinary open access archive for the deposit and dissemination of scientific research documents, whether they are published or not. The documents may come from teaching and research institutions in France or abroad, or from public or private research centers.

L'archive ouverte pluridisciplinaire **HAL**, est destinée au dépôt et à la diffusion de documents scientifiques de niveau recherche, publiés ou non, émanant des établissements d'enseignement et de recherche français ou étrangers, des laboratoires publics ou privés.

Astrophys Space Sci (2019) 364:58
https://doi.org/10.1007/s10509-019-3548-6

ORIGINAL ARTICLE

# MERcury Gravity REcovery and Analysis System (MERGREAS) and its performances from simulated four-way Doppler measurements

Jianguo Yan[1,2] · Shanhong Liu[1] · Xuan Yang[1] · Chi Xiao[3] · Mao Ye[1] · Weitong Jin[1] · Fei Li[1] · Jean-Pierre Barriot[1,4]

Received: 9 August 2018 / Accepted: 3 April 2019 / Published online: 9 April 2019
© Springer Nature B.V. 2019

**Abstract** The exploration of the planet Mercury requires software applications that can execute Precise Orbit Determination (POD) and estimate dynamic parameter solutions. In this paper, we present MERcury Gravity REcovery and Analysis System (MERGREAS), a new software product that is designed to support the future Chinese Mercury explorations. To validate the software we crosschecked the MERGREAS functionalities against the GEODYN-II. Simulated orbit determination experiments show that the differences between MERGREAS and GEODYN-II in the $X$, $Y$, and $Z$ directions were 0.2, 0.7, and 0.5 m respectively with the arc length of 24 h. The integration interval for both software platforms was 10s. The MERGREAS software can utilize four-way Doppler measurements for spacecraft orbit determination as well as precise positioning of a Mercury lander. In simulations, we show that when the four-way Doppler data are included, the accuracy in Mercury spacecraft orbit determination can reach the centimeter level and the lander positioning accuracy can be refined to decimeter level. Furthermore, when we considered the influence of the Mercury gravity errors, measurement bias, and Mercury orientation model errors in POD with MERGREAS, the errors in the orbiter position ranged as high as 300 meters with a lander position deviation of about 10 meters. The Mercury gravity field solution was improved and the accuracy of the Mercury tidal Love number $k_2$ increased by an order of magnitude when simulated four-way Doppler data were added. The more precise $k_2$ value enhanced the accuracy of the constraints used in internal physical parameters estimation for Mercury. These results provide a reference for future Chinese Mercury exploration missions.

**Keywords** Mercury · Two-way Doppler · Four-way Doppler · Precise orbit determination · Mercury tidal Love number

## 1 Introduction

Mercury with a diameter of 4878 km, is smaller than Earth but is the planet in the solar system closest in density to Earth. It has an intrinsic global magnetic field with a thin exosphere, composed of helium, oxygen, and sodium (Potter and Morgan 1985; Johnson and Hauck 2016). Due to its close proximity to the Sun and its highly elliptical orbit between 0.3 and 0.47 AU, Mercury is difficult to explore (Correia and Laskar 2004; Wieczorek et al. 2011).

The investigation of the topography, internal structure, material composition and atmospheric environment of Mercury will help us to understand the origin and evolution of the solar system (Ernst et al. 2010; Smith et al. 2012). The National Aeronautics and Space Administration (NASA) have completed two Mercury exploratory missions. Mariner

**Electronic supplementary material** The online version of this article (https://doi.org/10.1007/s10509-019-3548-6) contains supplementary material, which is available to authorized users.

✉ J. Yan
jgyan@whu.edu.cn

✉ M. Ye
mye@whu.edu.cn

1 State Key Laboratory of Information Engineering in Surveying, Mapping and Remote Sensing, Wuhan University, 129 Luoyu Road, Wuhan 430070, China

2 State Key Laboratory of Astronautic Dynamics, Xi'an Satellite Control Center, Xi'an 710000, China

3 Chinese Antarctic Center of Surveying and Mapping, Wuhan University, Wuhan 430079, China

4 Observatoire géodésique de Tahiti, BP 6570, 98702 Faa'a, Tahiti, French Polynesia

10, launched in 1973, completed the first successful Mercury flyby. In 2004, the Mercury Surface Space, Environment, Geochemistry, and Ranging (MESSENGER) mission was launched. After a nearly seven-year flight, it went into orbit around Mercury (Genova et al. 2013). The Japan Aerospace Exploration Agency (JAXA) and European Space Agency (ESA) cooperated to advance the Bepi-Colombo Mercury mission. This spacecraft was launched in 20, October 2018 and is expected to arrive at Mercury in December 2025 (ESA Media Relations Office 2018). China has also officially established an agenda for space exploration targeting asteroids, Mars, Jupiter and potential Mercury (The state council information office of China 2016). The development of a POD software system was, and will remain, an indispensable part of these Mercury missions.

The POD of the spacecraft provides the ephemeris necessary for terrain mapping and the Mercury gravity field modeling, and indispensable for investigation of the interior structure of this planet. Currently, there are four well-known high precision software platforms employed for processing Mercury spacecraft tracking data. These include the Orbit Determination Program (ODP) and subsequent Mission analysis, the Operations and Navigation Toolkit Environment (MONTE) software suite developed by JPL (Moyer 2001; Evans et al. 2016), and GEODYN-II developed by the Goddard Space Flight Center (GSFC) (Pavlis et al. 2000). In 2016, the University of Pisa developed the ORBIT14 software. This software was employed to estimate libration, amplitude obliquity, and the post Newton parameter from a tracking simulation of BepiColombo (Schettino and Tommei 2016; Cicalò et al. 2016). In consideration of the potential Chinese Mercury missions and the restriction of access to the existing software, the planetary geodesy research group of Wuhan University developed the software MERcury Gravity REcovery and Analysis System (MERGREAS) based on in-house software for lunar and Mars spacecraft POD solutions (Li et al. 2016; Yan et al. 2017). This paper introduces MERGREAS and assesses its potential performance in the proposed Mercury missions using GEODYN-II as a benchmark reference.

GEODYN-II has been widely used in planetary POD and dynamic parameters estimation in various lunar missions such as the Lunar Prospector, SELENE, the Lunar Reconnaissance Orbiter, and the Gravity Recovery and Interior Laboratory (Goossens et al. 2011; Lemoine et al. 2013). GEODYN-II was also used in Mars missions including the Mars Global Surveyor, Odyssey, and the Mars Reconnaissance Orbiter (Genova et al. 2016), and in the MESSENGER Mercury mission (Mazarico et al. 2014). The reliability and stability of GEODYN-II was demonstrated in these various missions. We used GEODYN II to evaluate the simulated observation and POD functions in MERGREAS. MERGREAS moreover, can handle four-way Doppler model, unlike other similar software products.

This four-way Doppler model was applied in SELENE mission to provide accurate tracking data of the lunar farside (Iwata et al. 2001; Namiki et al. 2009). This data successfully improved the main satellite's trajectory and retrieved lunar farside gravity information directly for the first time (Namiki et al. 2009). This four-way tracking mode is versatile and can be used in Mercury exploration. We simulated the four-way Doppler tracking data and investigated its contribution to Mercury spacecraft POD, precise positioning of the lander, the Mercury tidal $k_2$, and Mercury gravity field recovery.

Mercury tidal Love number $k_2$ is the efficiency of the response, in terms of gravity potential, of Mercury as forced by the degree-2 component. The $k_2$ potential Love number scales the tidal deformation of Mercury and is estimated from spacecraft orbital tracking data, as coupling $k_2$ with moment of inertia constrains the estimation of the Mercury core status (Rivoldini et al. 2009; Padovan et al. 2014). The $k_2$ value has improved significantly since the MESSENGER mission. Mazarico et al. (2014) used three years of MESSENGER tracking data and calculated $k_2$ as $0.451 \pm 0.014$. Verma and Margot (2016) presented a $k_2$ value of $0.464 \pm 0.023$ based on MESSENGER tracking data for the period March 2011 to April 2014. The contribution of the four-way tracking mode in our $k_2$ solution is considered in our work.

In this paper, we introduce the design and structure of the MERGREAS, and use MERGREAS to predict the Mercury spacecraft trajectory, generate synthetic two-way range and range-rate observations between an Earth tracking station and a Mercury spacecraft, and execute POD. We compare these results with those from the GEODYN-II reference software. We analyze the MERGREAS POD of the spacecraft, precise positioning of the Mercury lander, and evaluate the $k_2$ estimate by adding various model errors. Furthermore, we present a preliminary estimate of Mercury gravity field recovery as well as a $k_2$ solution based on the four-way mode and two-way mode. Finally, we also analyze the influence of $k_2$ on the interior structural parameters of Mercury.

## 2 MERGREAS function and its cross validation

In MERGREAS, the POD of a Mercury spacecraft and the solution for dynamic parameters are based on dynamic orbit determination theory (Tapley et al. 2004). MERGREAS was written in Fortran 90 and designed to be a comprehensive and flexible system for executing POD as well as estimating dynamic parameters to investigate the interior structure of Mercury. Currently, MERGREAS can accomplish the following tasks:

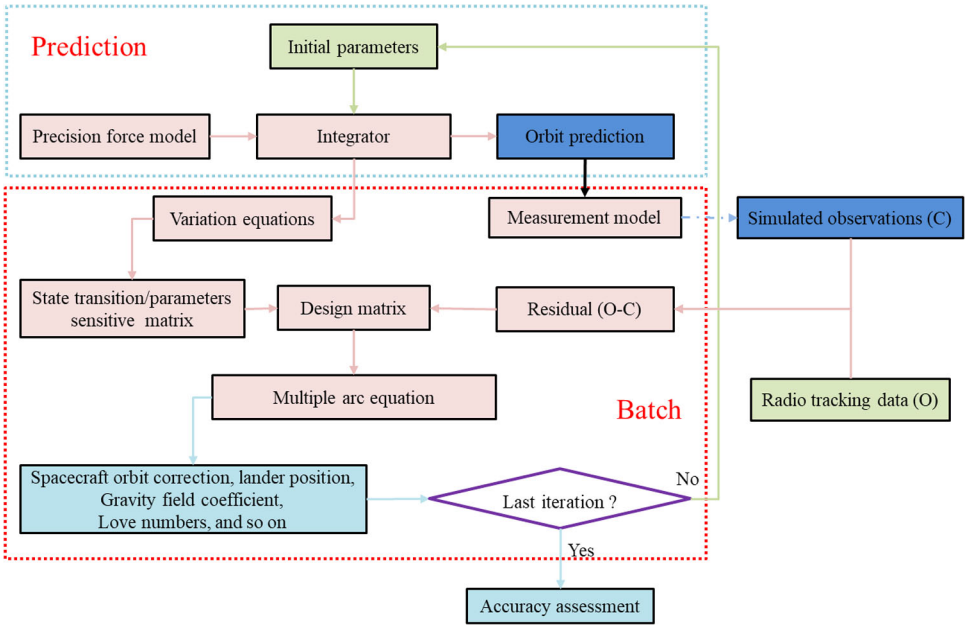


**Fig. 1** A flowchart of precise orbit determination (POD) and gravity field recovery in MERGREAS

(i) effectively predicts a Mercury spacecraft trajectory in light of all the possible perturbation force models.
(ii) generates simulated tracking data. MERGREAS can simulate tracking data from single or dual earth stations, e.g., one-way range-rate, two-way range/range-rate, three-way range/range-rate, VLBI delay/delay rate, same-beam VLBI, and four-way Doppler.
(iii) implements POD of the Mercury spacecraft, precise positioning of the lander, $k_2$ solution, and executes Mercury gravity field recovery.

A flowchart of MERGREAS is shown in Fig. 1. A 12-order Adams-Cowell prediction-correction integrator is used to combine dynamic and variation equations (Healy and Berry 2004) to obtain the spacecraft ephemeris, the state transition matrix and the parameter sensitivity matrix. The C is a theoretical value calculated from geometric model. Observations O are provided by Earth tracking stations. They are used to generate residuals for further weighted least-square batch processing. We obtain local parameter solutions for each arc using this weighted least square method, and then generate a normal matrix of global parameters. We combine each normal matrix to solve the global parameters (Kaula 1966). The whole process is iterated to obtain a converged solution.

## 2.1 Configuration for cross validation between MERGREAS and GEODYN-II

In cross validation tests, these two software systems predicted the trajectory of spacecraft using the same initial orbital elements. The initial orbital elements taken from the MESSENGER mission were retrieved from SPICE (Acton 1996; Acton et al. 2017). The configuration for cross validation between MERGREAS and GEODYN-II is shown in Table 1.

In Table 1, we list the force and observation correction models used in MERGREAS. These configurations were also used to create the simulated observations discussed in this paper. In following sections, we compare the trajectory predictions, simulated observations, and POD results produced by the MERGREAS and GEODYN-II software.

## 2.2 Trajectory prediction comparison

We predicted the spacecraft trajectory and compared our estimated orbits with those from GEODYN-II to assess the accuracy and reliability of trajectory prediction with MERGREAS. The initial orbital elements applied in this comparative assessment are given in Table 2. These results in turn are visualized in Fig. 2. The right side of the figure shows the positional difference in the predicted trajectory, while the left side shows the difference in velocity for six days, from 09–11 08:00:00 to 09–17 08:00:00, 2011 (UTC).

In Fig. 2, we can see that the difference of the predicted orbit position is in the magnitude of $10^{-7}$–$10^{-8}$ m, and the difference of predicted velocity is within $2.0 \times 10^{-10}$ m/s for arc length of one day. Even after six days, the difference of the predicted position is in the order of $10^{-5}$ m, and the difference of the predicted velocity is in the order of $10^{-8}$ m/s. These results approach the double precision limit of FORTRAN since the accurate trajectory computation in the Mercury body-fixed system only can be in the order of $10^{-7}$–$10^{-8}$ m. Thus, these results reveal that MERGREAS performs as well as GEODYN-II in orbital prediction.

**Table 1** The configuration of MERGREAS

| Item | Name | Detail information |
|---|---|---|
| Force models | Mercury gravity field | Hgm005 (Mazarico et al. 2014) |
| | N-body perturbation | DE430 (Williams et al. 2013) |
| | Solar radiation | Canon ball model (Montenbruck and Gill 2002) |
| | Relativity perturbation | Schwarzschild (Sun only) |
| Correction | Tracking station coordination correction | Earth solid tide, ocean tide and polar tide correction (Petit and Luzum 2010) |
| | Earth tropospheric correction | Saastamoinen model and Global Mapping Function GMF (Saastamoinen 1972; Böhm et al. 2006) |
| | The speed of light correction | Relativistic effect (Moyer 2005) |
| Others | TDB-TT translation model | Moyer (2001) |
| | Ground tracking station | Kashi (China) |
| | Cut-off angle | 10° |
| | Mercury rotation model | Mercury orientation model from IAU (Petit and Luzum 2010) |
| | Mercury inertial system | Mercury J2000 |

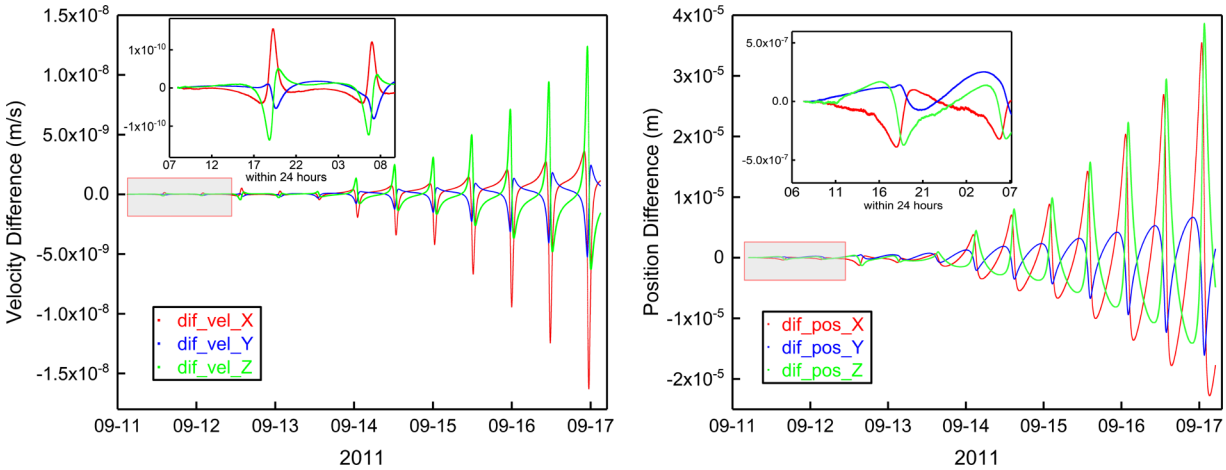


**Fig. 2** Trajectory prediction differences between MERGREAS and GEODYN-II. On the right side red, blue, and green points indicate $X$, $Y$, $Z$ position differences. On the left side, velocity differences are also shown as red, blue, and green points for $X$, $Y$, and $Z$

**Table 2** Initial orbital elements (2011-09-11 08:00:00)

| Items | Value |
|---|---|
| Perifocal distance (km) | 2640.246 |
| Eccentricity | 0.736 |
| Inclination (°) | 111.093 |
| Ascending node longitude (°) | 358.517 |
| Argument of periapse (°) | 107.021 |
| Mean anomaly (°) | 18.822 |

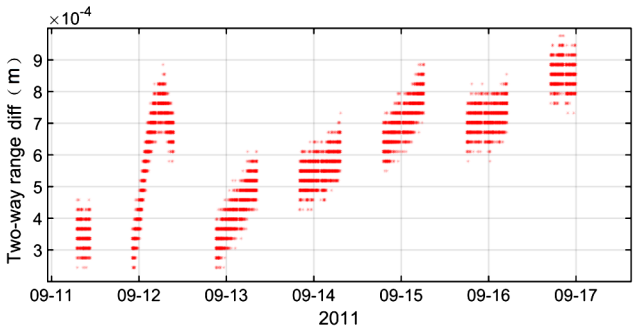


**Fig. 3** The simulated two-way range differences between MERGREAS and GEODYN-II

## 2.3 Simulation observations comparison

We simulated two-way range and range-rate observations to compare the differences in these two software systems. An antenna located at Beijing, China was used to generate the observations. We illustrate the differences in simulated two-way range (Fig. 3) and range-rate (Fig. 4) differ-

ences over a six-day period. We can see that the two-way range and range-rate difference between MERGREAS and GEODYN-II are less than $9 \times 10^{-4}$ m and $4.5 \times 10^{-6}$ m/s as shown in Figs. 3 and 4. In Fig. 3, the per time stamp corresponds to one point, and can be verified by enlarging this figure. The small difference between the MERGREAS and GEODYN-II results show that MERGREAS has the ability to generate simulated tracking data as accurately as GEODYN-II.

### 2.4 POD comparison

In POD cross validation experiments, we simulated two-way range-rate data for a spacecraft in a highly elliptical polar orbit; six arcs were selected to compare differences in the POD results. In order to make this POD comparison more rigorous and consistent for both GEODYN-II and MERGREAS, we executed POD with the same two-way range-rate data, but adding Gaussian noise (0.1 mm/s) generated from GEODYN-II.

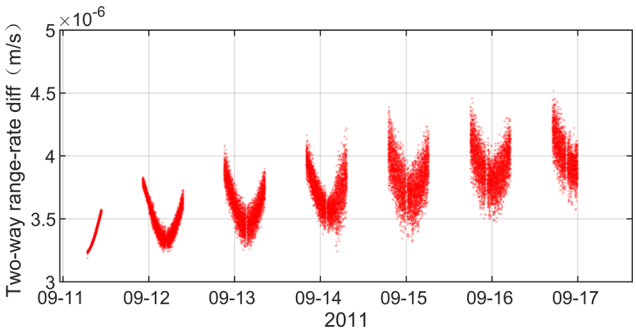


**Fig. 4** The simulated two-way range-rate differences between MERGREAS and GEODYN-II

Before executing POD, we added −100.0 m, 100.0 m, and −100.0 m to the initial orbital elements $X$, $Y$, $Z$ in the J2000 coordinates of Mercury. The POD results are listed in Table 3. The first six columns of Table 3 give the POD results. It can be seen that the differences are small as the maximum differences in $X$, $Y$, and $Z$ are 0.2, 0.7, and 0.5 m, respectively. The formal uncertainties of the initial orbit are given in the last six columns of Table 3. The formal uncertainties of the initial orbital values for MERGREAS and GEODYN-II are similar. These POD results demonstrate the consistency between MERGREAS and GEODYN-II.

Furthermore, we analyzed the two-way Doppler residuals for one arc in MERGREAS before and after POD. Figure 5 illustrates the prefit and postfit residuals for the two-way Doppler measurements. In Fig. 5 we see that the residuals decreased and without systematic error after POD. As expected, the residuals after POD had a 0.1 mm/s noise level. These results also confirm the reliability of MERGREAS orbit determination performance.

## 3 Four-way Doppler tracking mode

This section describes a measurement scenario of the four-way Doppler tracking mode. The two-way range and range-

**Table 3** Corrections and formal uncertainties of initial orbit for POD (m)

| No. Arc | Corrections | | | | | | Formal uncertainties | | | | | |
|---|---|---|---|---|---|---|---|---|---|---|---|---|
| | GEODYN-II (0.1 mm/s) | | | MERGREAS (0.1 mm/s) | | | GEODYN-II (0.1 mm/s) | | | MERGREAS (0.1 mm/s) | | |
| | $\Delta X$ | $\Delta Y$ | $\Delta Z$ | $\Delta X$ | $\Delta Y$ | $\Delta Z$ | $\Delta X$ | $\Delta Y$ | $\Delta Z$ | $\Delta X$ | $\Delta Y$ | $\Delta Z$ |
| 1 | 101.2 | −97.0 | 98.6 | 101.3 | −96.6 | 98.6 | 4.27 | 11.36 | 3.60 | 4.11 | 10.90 | 3.33 |
| 2 | 108.1 | −82.2 | 101.6 | 108.1 | −81.9 | 101.8 | 8.49 | 18.74 | 2.76 | 8.67 | 19.18 | 2.82 |
| 3 | 115.6 | −66.3 | 111.2 | 115.7 | −66.1 | 111.1 | 10.44 | 23.36 | 7.91 | 9.96 | 22.19 | 7.49 |
| 4 | 91.8 | −117.7 | 92.1 | 91.6 | −118.4 | 91.7 | 12.73 | 29.87 | 13.42 | 11.88 | 27.86 | 12.54 |
| 5 | 98.0 | −103.9 | 97.8 | 98.2 | −103.4 | 98.0 | 19.65 | 37.40 | 19.63 | 13.8 | 34.59 | 18.17 |
| 6 | 101.6 | −95.5 | 102.4 | 101.5 | −96.2 | 101.9 | 17.13 | 46.52 | 26.96 | 15.62 | 42.45 | 24.61 |

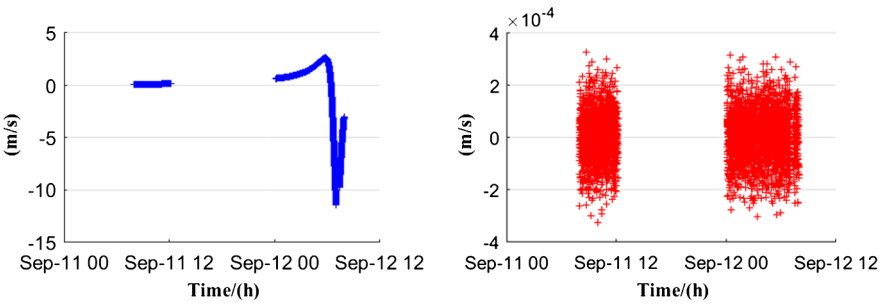


**Fig. 5** Residuals of two-way Doppler in MERGREAS. The left column is pre-fit residuals, and the right column is post-fit residuals

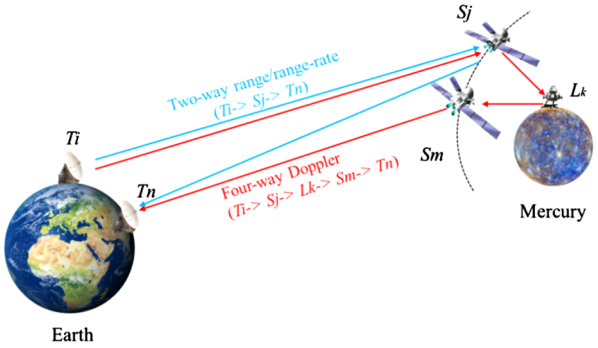


**Fig. 6** Four-way Doppler mode (red) and Two-way range and range-rate mode (blue)

rate (Thornton and Border 2003), and four-way Doppler were shown in Fig. 6.

In contrast to the traditional two-way mode, this four-way tracking mode adds an extra link between the lander and the spacecraft as shown in Fig. 6. In this measurement link, the Earth tracking station sends an uplink signal to a Mercury spacecraft. After the spacecraft receives the signal, it will transmit the signal to the Mercury lander at epoch. Subsequently the lander will transmit it to the spacecraft at epoch and the Earth station will receive it at epoch. In our simulation, we did not consider device hardware delay during signal transmission such as the transponder delay of probes, which would be calibrated on the ground before launch (Bertone et al. 2017). The four-way Doppler is computed by differencing four-way range with time intervals; the four-way range can be obtained in this form:

$$\begin{aligned} R &= (R_1 + c \cdot RLT_{nm}) + R_2 + R_3 + (R_4 + c \cdot RLT_{ij}) \\ &\quad + c \cdot \left[TDB(i) - UTC(i)\right] \\ &\quad - c \cdot \left[TDB(n) - UTC(n)\right] \\ &= c \cdot \left[UTC(n) - UTC(i)\right] \end{aligned} \tag{1}$$

$$R_1 = |X(S_m) - X(T_n)| \tag{2}$$

$$R_2 = |X(S_m) - X(L_k)| \tag{3}$$

$$R_3 = \left|X(S_j) - X(L_k)\right| \tag{4}$$

$$R_4 = \left|X(S_j) - X(T_i)\right| \tag{5}$$

Where $R_1$, $R_2$, $R_3$, and $R_4$ represent the geometric distance and $X(S_m)$ represents the position vector of the participant $m$ in the Barycentric Celestial Reference System (BCRS), similar to $X(S_j)$, $X(T_i)$, $X(T_n)$, and $X(L_k)$. $RLT_{nm}$ and $RLT_{ij}$ are the Shapiro delay for the Mercury spacecraft to station $T_2$ and $T_1$ (Shapiro 1964; Moyer 2005; Tommei et al. 2010). The computation of the range-rate is normally expressed in the integral Doppler form. In one Doppler integration period, the range-rate measurement can be described as the rate of the distance change between the start time $T_s$ and the end time $T_e$. At time $T_s$ and $T_e$, $R_s$ and $R_e$ are obtained by Eq. (1). The range-rate can be expressed as,

$$\dot{R} = \frac{R_e - R_s}{T_e - T_s} \tag{6}$$

Based on Eqs. (1)–(6) we generated the four-way Doppler data, and used these data in Mercury spacecraft POD and lander positioning. As the four-way Doppler data can be linked to the Mercury surface directly, it is also sensitive to Mercury tidal Love number $k_2$.

## 4 Solving $k_2$ and lander position using four-way Doppler data

The Qingdao station in China was chosen for generating the simulated four-way Doppler data. The simulation time length was set from 2021-10-01 00:00:00 to 2021-12-01 00:00:00 (UTC). We located the lander on Mercury at 3.139°E, and 58.845°N. When simulating four-way Doppler data we set $k_2$ with 0.451 as true value and an error bar of 0.014 (Mazarico et al. 2014). Gaussian white noise with an RMS value of 0.1 mm/s or 0.5 mm/s was added to the simulated four-way Doppler to study its influence on the results.

To solve the lander position and $k_2$ in a realistic scenario, we considered various error sources, including the gravity field errors, measurement bias, and orientation model error. To account for these error sources, we designed four strategies, termed case A, B, C, and D, to test how these error sources influence POD.

(i) Case A did not include gravity errors, measurement bias and Mercury rotation model error.
(ii) Case B included measurement bias (1 mm/s).
(iii) Case C had gravity errors with three times uncertainty and measurement bias (1 mm/s).
(iv) Case D included gravity errors with three times the uncertainty, measurement bias (1 mm/s), and orientation model error.

Stark et al. (2015) solved the uncertainty in the Mercury orientation model, so we referred to this work when adding error to our Mercury orientation model thus; $\alpha_0 = 281.0097 + 0.0012$ and $\delta_0 = 61.4143 + 0.00072$, these values are the ICRF equatorial coordinates from epoch J2000.0.

### 4.1 Sensitiveness analysis for $k_2$

Case A focused on the contribution of the four-way tracking data in spacecraft orbit determination and its sensitivity in the $k_2$ solution. We ignored gravity errors, measurement bias and Mercury rotation model error, which is the ideal situation and can achieve the theoretic results of the four-way mode. Figures 7(a)–(g) show the partials from one arc. The

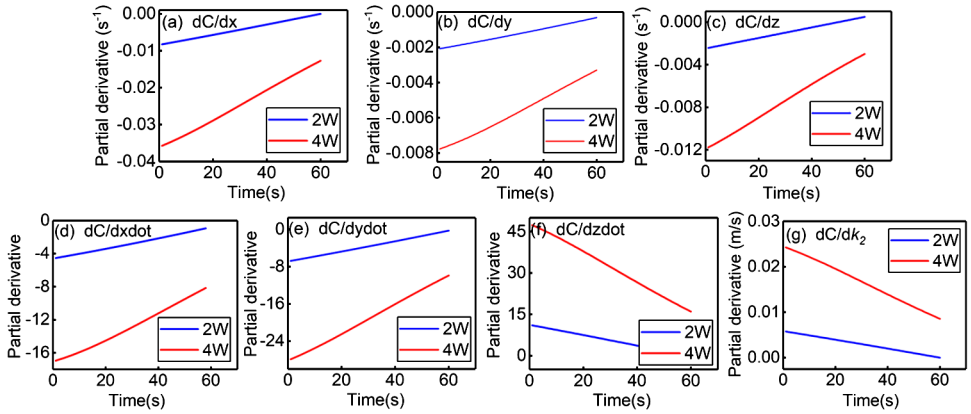


**Fig. 7** The partials of two-way and four-way observables with respect to the initial states and $k_2$ in one arc. C: observation of theoretical calculation; x: the x axis value of spacecraft; y: the y axis value of spacecraft; z: the z axis value of spacecraft; xdot: the x axis value of spacecraft velocity; ydot: the y axis value of spacecraft velocity; zdot: the z axis value of spacecraft velocity; $k_2$: Love number

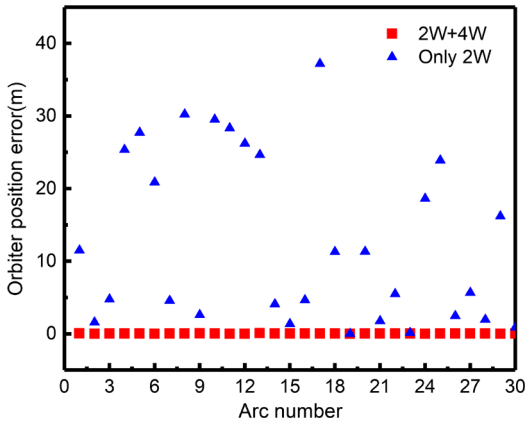


**Fig. 8** Position correction error in the initial orbit of each arc. Blue points are the results from 2W data; red points are the results from 2W + 4W data

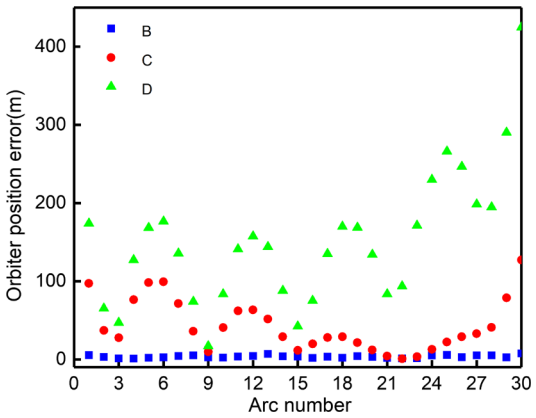


**Fig. 9** Position correction of initial orbit of each arc used 2W + 4W

absolute value of the red line is always larger than the blue line, which indicates the four-way observables were more sensitive to the initial state and $k_2$ than two-way observables.

## 4.2 POD, $k_2$ and lander position solution considering different error sources

We considered various error sources and analyzed the influence in POD, lander position and $k_2$ solution in case B, C, and D. We set *a priori* $k_2$ value to 0.1 and added 100 m of deviation to the $X$ and $Z$-axis of the lander position in body-fixed coordination of Mercury before POD in these simulation experiments. We obtained similar results after adding error on the $Y$-axis.

As the true orbital elements were known in this simulation, POD accuracy was assessed based on the differences between the reconstructed orbital elements and the true orbital elements. The spacecraft POD solutions of Case A under an ideal situation are shown in Fig. 8. We used both the two-way Doppler and four-way Doppler data in the simulation, these results are labeled as '2W + 4W'; the results using only the two-way Doppler data in the simulation are labeled, 'Only 2W'. Figure 8 indicates the improvement after the four-way Doppler data were added. The RMS of the spacecraft position error was 5.88 m when using only two-way data, while the error was reduced to 0.032 m after three iterations, when the four-way data were included. Figure 9 shows the spacecraft orbital error in case B, C, D. Case D had the most complex model errors, including gravity field errors with three times uncertainty, measurement bias (1 mm/s), and orientation model error. In Fig. 9 we can see that the added measurement bias in case B led to meter error level in the spacecraft orbit. With the added field gravity errors and measurement bias in case C, the orbital accuracy was about 100 m; while in case D with the gravity errors, measurement bias, and orientation model error, the orbital accuracy reached the 300 m level.

Furthermore, we selected an arc to compare the orbital differences. Figure 10 illustrates orbital differences between the true orbit and the reconstructed orbit from the four cases. From Fig. 10, we can see that when measurement bias and gravity errors were added, the difference in error between reconstructed orbit and true orbit was small in cases B and C. However, the error between the reconstructed orbit and true orbit was 0.4 km in case D. Thus, orientation model error has a larger influence on the orbiter position than the influence

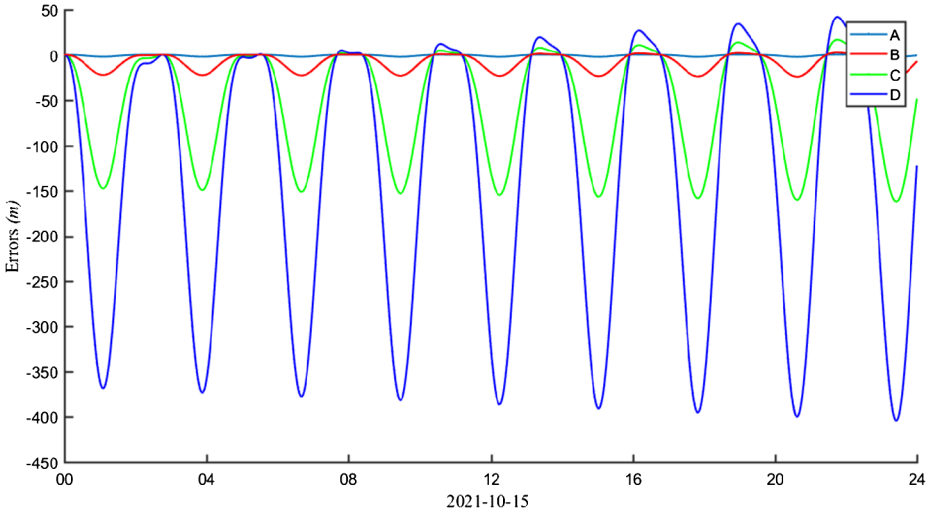


**Fig. 10** The norm of the difference in the position vectors between true orbit results and reconstructed orbits (2W + 4W)

**Table 4** Lander position correction value using four-way Doppler (4W) combined with two-way range-rate (2W) (m)

| Strategies | Iteration number | 2W (0.1 mm/s) + 4W (0.1 mm/s) (30 days) | | | 2W (0.1 mm/s) + 4W (0.1 mm/s) (60 days) | | | 2W (0.1 mm/s) + 4W (0.5 mm/s) (60 days) | | |
|---|---|---|---|---|---|---|---|---|---|---|
| | | *X* | *Y* | *Z* | *X* | *Y* | *Z* | *X* | *Y* | *Z* |
| A | 1 | −100.010 | −0.013 | 100.008 | −100.007 | 0.011 | 100.007 | −100.900 | −0.010 | 100.046 |
| | 2 | 0.009 | 0.001 | −0.007 | 0.004 | −0.004 | −0.003 | 0.005 | 0.003 | −0.001 |
| | 3 | −0.000 | 0.000 | 0.003 | −0.000 | 0.001 | −0.005 | −0.000 | 0.001 | −0.005 |
| | Total | −100.000 | −0.012 | 100.004 | −100.003 | 0.008 | 99.999 | −100.895 | −0.006 | 100.040 |
| | SD | 0.059 | 0.041 | 0.065 | 0.035 | 0.031 | 0.067 | 0.052 | 0.048 | 0.062 |
| B | 1 | −100.109 | −0.196 | 100.594 | −100.131 | −0.102 | 100.145 | −98.873 | −0.072 | 101.061 |
| | 2 | −0.014 | 0.023 | 0.244 | −0.017 | 0.007 | 0.197 | 2.094 | 0.078 | −0.366 |
| | 3 | 0.005 | 0.002 | 0.001 | 0.004 | 0.001 | 0.001 | −1.008 | 0.013 | 0.024 |
| | Total | −100.118 | −0.171 | 100.839 | −100.144 | −0.094 | 100.343 | −97.787 | 0.019 | 100.719 |
| | SD | 0.054 | 0.039 | 0.084 | 0.036 | 0.028 | 0.038 | 0.038 | 0.035 | 0.036 |
| C | 1 | −98.102 | −9.146 | 95.457 | −100.128 | −0.189 | 100.153 | −98.628 | −0.089 | 100.553 |
| | 2 | 0.587 | −0.426 | −2.182 | 0.225 | 0.113 | 0.287 | 0.425 | 0.019 | 0.025 |
| | 3 | 0.311 | −0.287 | −0.248 | 0.012 | −0.032 | 0.012 | 0.001 | −0.251 | 0.007 |
| | Total | −97.204 | −9.859 | 93.028 | −99.891 | −0.108 | 100.452 | −98.202 | −0.321 | 100.585 |
| | SD | 0.143 | 0.151 | 0.158 | 0.076 | 0.081 | 0.075 | 0.076 | 0.081 | 0.075 |
| D | 1 | −105.230 | −6.802 | 135.693 | −101.505 | 0.174 | 100.614 | −98.505 | −0.174 | 100.614 |
| | 2 | −2.005 | −3.566 | −22.625 | 0.642 | 0.008 | −0.112 | −0.435 | −0.028 | −0.036 |
| | 3 | −1.655 | −1.626 | −8.478 | 0.061 | −0.006 | 0.021 | 0.165 | −0.005 | 0.004 |
| | Total | −108.890 | −11.994 | 104.590 | −100.802 | 0.176 | 100.523 | −98.775 | −0.207 | 100.582 |
| | SD | 0.237 | 0.237 | 0.726 | 0.071 | 0.083 | 0.068 | 0.078 | 0.081 | 0.075 |

Note: Standard deviation (SD)

of errors in the gravity field coefficient and measurement bias. One possible reason for this could be that orientation error affects the lander and orbiter positions during coordinate transformation.

The iterative process that solves the lander position is shown in Table 4. A convergent result was achieved after three iterations. In Table 4, we present the results from the four cases A, B, C, and D. In our experiments, we simulated 30- and 60-day periods considering the rotation period of Mercury (about 59 days). Table 4 demonstrates that if we solve the Mercury lander position value using a 30-day length of observation data with 0.1 mm/s of noise in both

**Table 5** The simulation POD result of $k_2$

| Strategies | 2W (0.1 mm/s) (30 days) | 2W (0.1 mm/s) + 4W (0.1 mm/s) (30 days) | 2W (0.1 mm/s) (60 days) | 2W (0.1 mm/s) + 4W (0.1 mm/s) (60 days) | 2W (0.1 mm/s) + 4W (0.5 mm/s) (60 days) |
|---|---|---|---|---|---|
| A | $0.455 \pm 0.05$ | $0.451 \pm 0.03$ | $0.451 \pm 0.03$ | $0.451 \pm 0.02$ | $0.451 \pm 0.02$ |
| B | $0.413 \pm 0.05$ | $0.423 \pm 0.04$ | $0.451 \pm 0.03$ | $0.451 \pm 0.02$ | $0.449 \pm 0.02$ |
| C | $0.401 \pm 0.05$ | $0.476 \pm 0.05$ | $0.595 \pm 0.03$ | $0.501 \pm 0.02$ | $0.592 \pm 0.02$ |
| D | $0.369 \pm 0.05$ | $0.465 \pm 0.04$ | $0.606 \pm 0.03$ | $0.600 \pm 0.02$ | $0.662 \pm 0.02$ |

the two-way and four-way data, as in case A, the lander position error can be reduced to the centimeter level. In case B however, error in the lander position reached the meter level. When we considered the gravity errors and measurement bias, the lander position error rose to about the ten meter level as shown in case C. In case D, the lander position error was approximately 12 m. In Table 4, we also present a lander positioning solution with longer tracking data simulated for a 60-day period. With this length data, the lander position error was at decimeter level in the case A with 0.5 mm/s noise for the four-way data and 0.1 mm/s for the two-way data, as shown in Table 4. In cases B, C, and D, the lander position error was at about the meter level. This experiment demonstrates that data collected over a longer time can help to solve the lander position, even when we consider multiple types of model error.

We investigated the applicability of the four-way mode observations when calculating a $k_2$ solution in the 30-day period, as detailed in Table 5. The actual delta value (the deviation from the true $k_2$ value) was improved by about one order of magnitude. The result based on the two-way data was $0.4551 \pm 0.05$ (1-sigma) with a delta of 0.0041, when compared to the true $k_2$ value. After combining the two-way data with the four-way data, the resulting $k_2$ value was $0.4515 \pm 0.03$ (1-sigma) with a delta of 0.0005, when compared to the true $k_2$ value. The various error sources, including measurement bias, orientation model error, and gravity field error degraded the $k_2$ solution. However, in cases B and C, we can see the four-way data can improve the $k_2$ solution to some extent, possibly due to its more sensitivity to $k_2$ as shown in Fig. 7(g).

We also studied the influence of the longer measurement time and higher noise level in the four-way data on $k_2$ estimation. As shown in the last two columns of Table 5 we can see that the longer observation time improved the solution accuracy of $k_2$ in cases A and B, using only the two-way data. With a longer measurement time the influence of measurement bias was reduced, however, the gravity and rotation errors still degraded the $k_2$ solution. At the same time, we found that after we increased the noise level in the four-way data, its contribution in the $k_2$ solution was not significant. If we include the errors from measurement bias and the orientation model, the $k_2$ solutions deteriorated even further, as indicated by the results from cases C and D.

## 5 Mercury gravity field recovery using four-way Doppler data

### 5.1 Mercury gravity field and $k_2$ solution

We further demonstrate MERGREAS capabilities in Mercury gravity field recovery by using both the two-way and four-way data. In this simulation, the $k_2$ was solved simultaneously with the gravity field coefficients. The sigma of the Gaussian noise added to the measurement for both the two-way and four-way tracking data was 0.1 mm/s. The single arc length in these solutions was one day. We chose a circular polar orbiter at a height of 800 km. We selected the first degree and order 20 from Hgm100 as the true model, called "Hgm20" hereafter. The *a prior* model applied in this gravity field solution was generated from the Hgm20 by adding the formal uncertainty of the coefficients to its value. We achieved a convergent gravity field solution and $k_2$ value after three iterations in this test, and the Kaula constraint was not employed (Kaula 1966). Moreover, in order to focus the Mercury gravity field recovery in four-way mode, the error of the Mercury rotation model was not included in this section.

Figure 11 shows the power spectrum curves of the estimated gravity models for different data lengths and tracking data. The RMS coefficient sigma degree variance $\sigma_n$ is labeled "$\sigma$" and RMS coefficient error degree variance $\delta_n$ is labeled "$\delta$" and the signal difference degree-RMS is labeled "$\Delta$", in Fig. 11. The formulas used for computing these values are as follows (Kaula 1966):

$$\begin{aligned}
\sigma_n &= \sqrt{\frac{\sum_{m=0}^{n}(\overline{C}_{nm}^2 + \overline{S}_{nm}^2)}{2n+1}}, \\
\delta_n &= \sqrt{\frac{\sum_{m=0}^{n}(\sigma_{\overline{C}_{nm}}^2 + \sigma_{\overline{S}_{nm}}^2)}{2n+1}}, \\
\Delta_n &= \sqrt{\frac{\sum_{m=0}^{n}(\Delta\overline{C}_{nm}^2 + \Delta\overline{S}_{nm}^2)}{2n+1}}
\end{aligned} \tag{7}$$

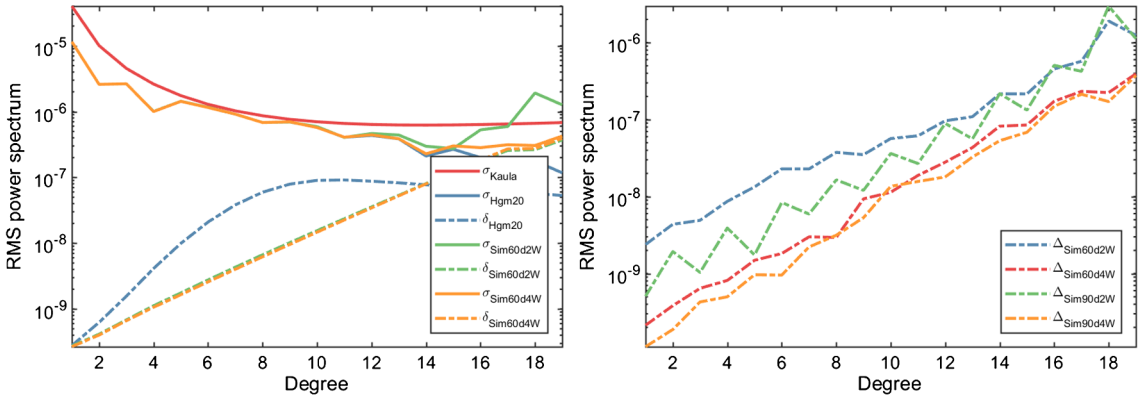


**Fig. 11** Power spectra of gravity field solutions. Non-marked solid lines: signal degree-RMS (labeled "$\sigma$") and dashed lines: formal error degree-RMS (labeled "$\delta$"); marked dashed lines: signal difference degree-RMS (labeled "$\Delta$") with respect to the "true" model Hgm20; the red curve corresponds to Kaula's rule, $4 \times 10^{-5}/l^2$

where $\sigma^2_{\overline{C}_{nm}}$ and $\sigma^2_{\overline{S}_{nm}}$ are error variances of the normalized Stokes coefficients $\overline{C}_{nm}$ and $\overline{S}_{nm}$, respectively; $\Delta\overline{C}^2_{nm}$ and $\Delta\overline{S}^2_{nm}$ denote differences between gravity field coefficients. The variances in RMS coefficient sigma degrees show the frequency intensity of the gravity field model. The variances in RMS coefficient error degree are formal errors in the posteriori covariance matrix of the model. The RMS coefficients difference degree variances indicate the deviations between these two models.

The gravity field solution requires more parameters than the lander positioning and $k_2$ solution, therefore a longer period of tracking data is required. We considered tracking lengths of 60 days and 90 days in gravity field recovery. The power spectrum of the gravity field models solved using different data lengths are presented in Fig. 11. For simplicity, we present the results from 60 days (labeled as "Sim60d2W") and 90 days (labeled as "Sim90d4W") of simulated data. The labels "2W" or "4W" were added to indicate if the solution was from two-way racking data, or the two-way plus four-way tracking data. From the left figure in Fig. 11, we can see that the gravity field improved slightly after we used the simulated tracking data from a longer time span. The contribution of the four-way data in the formal error is hard to discern graphically, which is consistent with the relatively small amount of influence from the four-way tracking data in the gravity field solution. This formal error is dependent on the number of observations. However, from the graph on the right side in Fig. 11 we can clearly see the contribution of the longer tracking time and four-way data in Mercury gravity field recovery. Even though the amount of the four-way data was only about 10% of the two-way data, the gravity field was improved by almost an order of magnitude after we included it in the solution. As we did not include the *Kaula* constraint in the gravity field solution, we can see that the formal uncertainty at the higher degrees (after degree 16) was larger than the coefficient degree variance.

Furthermore, we used the solved models to execute POD to evaluate the performance of various gravity field models. We used only two-way data to validate the improvement in the gravity field solution. We assessed the POD with the orbital difference, defined as the difference between the orbital solution from the solved model and the true orbital elements. After we used the Mercury gravity field solution including the four-way data, the orbital accuracy improved significantly (the RMS was 113.4 m for Sim90d2W, and 10.9 m for Sim90d4W), with an RMS of 1.6 m between the solution and the true Hgm20 models.

We solved the $k_2$ simultaneously with our gravity field solution to study the contribution of the four-way data. The $k_2$ solutions for four scenarios are listed in Table 6. The RMS expresses the formal error in the $k_2$ solution, while the deviation is the difference between the solution and priori true value. From Table 6 we can clearly see that the accuracy of the $k_2$ solution can be improved by at least an order of magnitude, after including the four-way data. Furthermore, Table 6 indicates that data collected over a longer time would also help to retrieve the $k_2$ information more accurately.

The correlations between $k_2$ and the Mercury gravity coefficients are displayed in Fig. 12. From Fig. 12, we can see that the correlation values in general are small. The correlation values for $k_2$ and Sim60d4W are smaller than Sim60d2W. The correlation values between $k_2$ and Sim90d4W are the smallest among these four scenarios, especially for those correlation values between the $k_2$ and the zonal coefficients. The decrease in the correlation values for $k_2$ and the Sim90d4W model could be due to the longer time span included in the data set and the inclusion of the four-way data.

**Table 6** The $k_2$ results with time length of 60 days and 90 days

| Time length | 2W | | | 2W + 4W | | |
|---|---|---|---|---|---|---|
| | $k_2$ | RMS | Deviation | $k_2$ | RMS | Deviation |
| 60-day | 0.45568 | 0.886E-03 | 0.00468 | 0.45144 | 0.643E-03 | 0.00044 |
| 90-day | 0.44885 | 0.381E-03 | 0.00215 | 0.45098 | 0.227E-03 | 0.00002 |

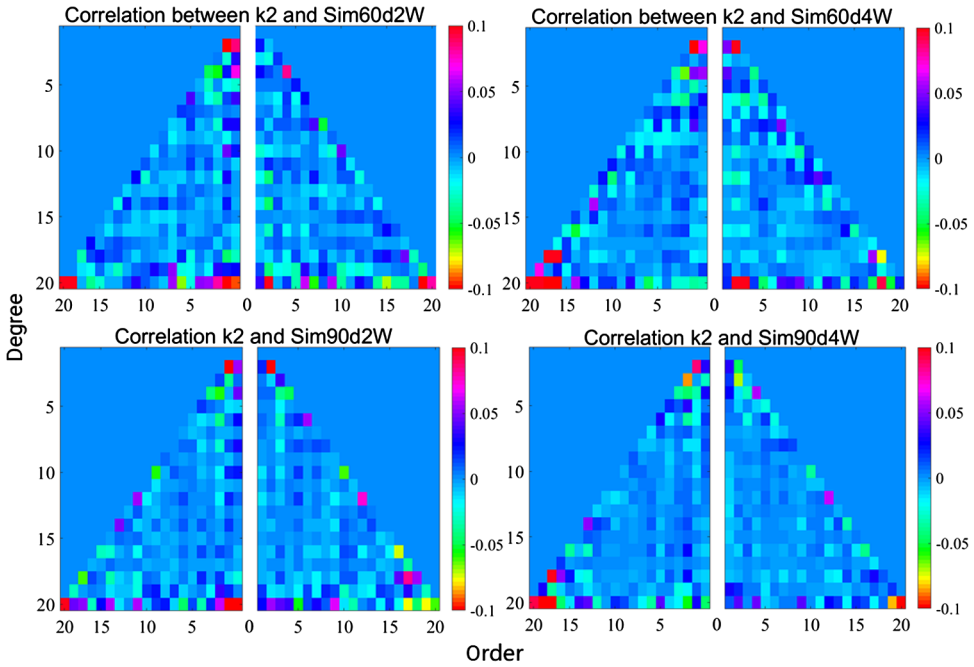


**Fig. 12** Correlation between $k_2$ and various gravity field models. For each plot the left part is correlation between the $k_2$ and *Cnm* coefficients, and the right part is correlation between the $k_2$ and *Snm* coefficients

## 5.2 Influence analysis of $k_2$ for Mercury interior structure parameters

The tidal response of Mercury is a function of the density, rigidity, and viscosity of the interior of the planet. The interior of the planet is characterized by the tidal Love number $k_2$, which is an effective indicator of the deep interior structure of Mercury (Van Hoolst and Jacobs 2003; Van Hoolst et al. 2007; Rivoldini et al. 2009; Mazarico et al. 2014). In this section, we study the response of the Love number $k_2$ obtained by different tracking modes on internal structural parameters. We assume that Mercury is in hydrostatic equilibrium (Rivoldini et al. 2009). As $k_2$ is a global parameter and represents response of the planet to tidal forcing, it is not sensitive to fine density structures (Padovan et al. 2014). Thus, we divided Mercury into four spherically symmetric layers: the inner core, outer core, mantle and crust. The density of crust and mantle and the crustal thickness were set as the values, 3200 kg/m$^3$, 3300 kg/m$^3$ and 100 km, respectively (Rivoldini et al. 2009). Based on Rivoldini and Van Hoolst (2013), and Dumberry and Rivoldini (2015), we assume that the range of the Core Mantle Boundary (CMB) is 1950–2050 km, the range of the Inner Core Boundary (ICB) is 500–1500 km, the range of outer core density is 6500–7500 kg/m$^3$, and the range of inner core is 8000–9000 kg/m$^3$ in our experiments. The equation used in our sensitive analysis is as follows (Khan et al. 2017),

$$\{R_{layer}, \rho_{layer}, V_P, V_S, \mu\} \xrightarrow{\text{operator}} \{k_2\} \tag{8}$$

where $R_{layer}$, $\rho_{layer}$, $V_P$, $V_S$, and $\mu$ are layer radius, density, $P$-wave velocity, $S$-wave velocity and viscosity for each layer. The operators represent the forward models as in Takeuchi and Saito (1972), and the detailed equations are presented in online supplementary.

We designed three cases to display the response of $k_2$ on Mercury interior structure parameters. In case one, we set a value of the ICB to 1000 km and changed the density of the inner core from 8000–9000 kg/m$^3$ so under different CMB conditions, the CMB varied from 1950 to 2010 km. In case two, we set a value of the ICB to 1000 km and changed the density of outer core from 6500–7500 kg/m$^3$ under different CMB conditions. In case three, we set a value of the density of inner core to 8970 kg/m$^3$ and changed the ICB from 500–1500 km under different CMB conditions. We present the results from these cases in Fig. 13.

Figures 13(a) and (b) show the results of case one. The density of inner core changed from 8220 to 9000 kg/m$^3$ so

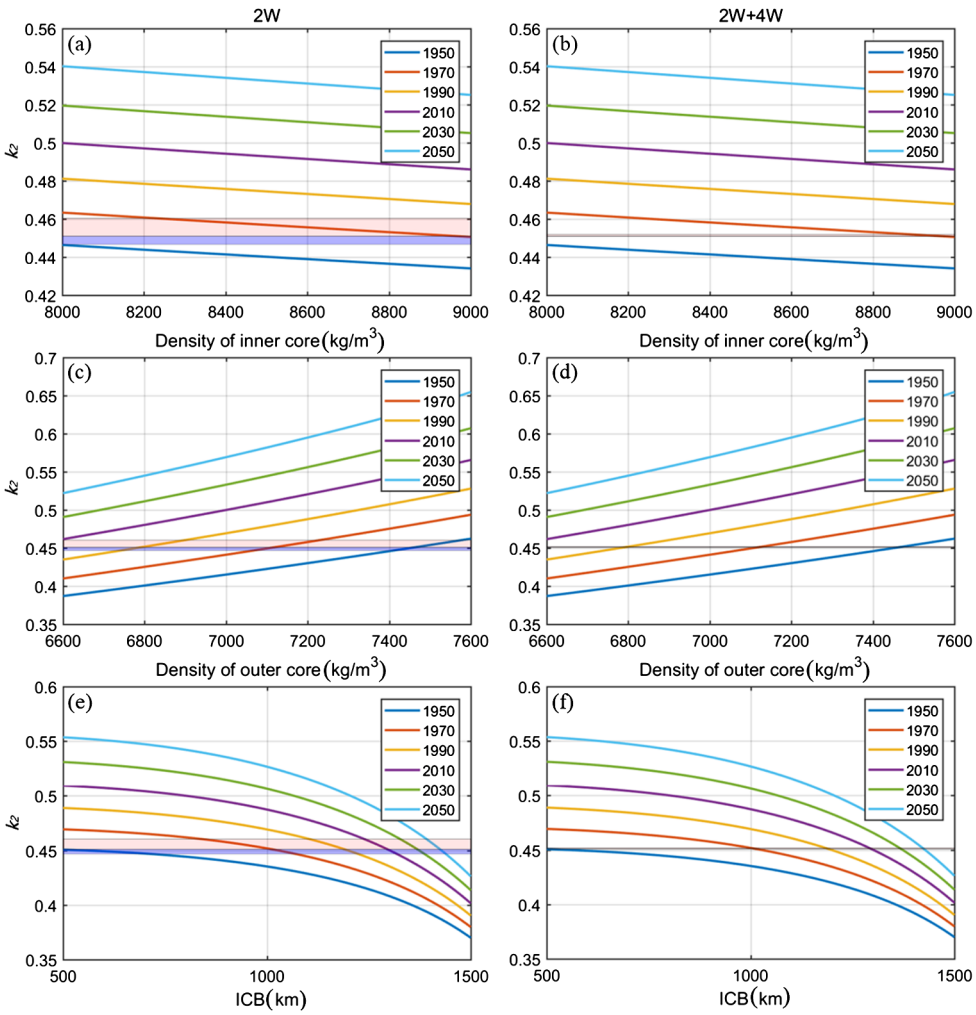


**Fig. 13** Influence of $k_2$ for Mercury interior structure parameters. The left rows are results from the $k_2$ of 2W mode, and right row are from the $k_2$ of 2W + 4W mode. (a) and (b): fixed the value of ICB with 1000 km and swept the density of inner core from 8000–9000 kg/m$^3$; (c) and (d): fixed the value of ICB with 1000 km and swept the density of outer core from 6500–7500 kg/m$^3$; (e) and (f): fixed the value of density of inner core with 8970 kg/m$^3$ and swept the ICB from 500–1500 km with different CMB conditions

a CMB of 1970 km can satisfy the Love number $k_2$ as obtained by the two-way mode. In the two-way and four-way mode combination, with a CMB of 1970 km, only the density of inner core ranging from 8890 to 8970 kg/m$^3$ can satisfy the Love number value, as the constraint on the density of the inner core is tightened by one order of magnitude.

Figures 13(c) and (d) show that in case two, with the CMB varying from 1950 to 2010 km, different ranges of density of the outer core can satisfy the $k_2$ obtained by the two-way mode. For the $k_2$ calculated from the two-way and four-way mode combination, we rejected the CMB with 2010 km, as the constraint interval on the density of outer core shrank sharply.

Figures 13(e) and (f) show the results of case three. Owing to our simplified model, each CMB had a range of ICB to satisfy the $k_2$. However, we find that when the CMB was selected as 1970 km as in test one, and then the ICB ranged from 840 km to 1040 km with the two-way mode and from 1000 km to 1015 km for the combination mode. As compared to two-way mode, the $k_2$ obtained by combination mode reduced the constraints on the ICB by almost one order of magnitude.

From these three tests, we can see that the tidal Love number $k_2$ obtained by the combination modes significantly improved the constraints on interior parameters of Mercury. However, this is only a specific result based on our assumption. The exactly error bar of density and radius cannot be provided since we know little about Mercury interior structure and physical parameters at the very beginning stage. After the BepiColombo mission, we may have chance to obtain higher accurate parameters related to interior structure related parameter, such as $k_2$ and low degree gravity field coefficients, and the error bar of density and boundaries will be more meaningful and achievable.

## 6 Conclusions

In this paper, we demonstrate the reliability of the MERGREAS Mercury precise orbit determination software in cross validation experiments. In these simulation experi-

ments, MERGREAS results were rigorously compared with results from the GEODYN-II reference software in terms of orbital prediction, observation data and POD. These results indicate the feasibility of MERGREAS for processing real data.

Another goal of this study was to investigate the potential contribution of the four-way Doppler data in Mercury lander precise positioning, estimating the Mercury tidal Love number $k_2$ and gravity field recovery. After combining simulated four-way Doppler data with traditional two-way Doppler data, the accuracy of Mercury spacecraft orbit determination was improved. When we added gravity error, measurement bias, and orientation model error, the lander position error rose to about the ten-meter level and the spacecraft orbital error to about 300 m. The $k_2$ solution however, was improved by around one order of magnitude with the help of four-way Doppler data under ideal conditions. When we considered various models error sources, the four-way tracking data reduced the uncertainty in the $k_2$ solution. A primary Mercury gravity field simulation was implemented to validate MERGREAS capabilities; these simulations confirmed that the four-way tracking data would significantly improve gravity field recovery and $k_2$ estimation. Moreover, the Love number $k_2$ obtained by the two-way and four-way mode combination significantly improved the constraints on internal parameters of Mercury. These results indicate the potential applications of the four-way tracking mode in future Chinese Mercury exploration missions. However, the study of interior structure of Mercury is one typical non-unique problem. The knowledge of the interior of Mercury will advance not only by increasing the $k_2$ accuracy but also by improving the accuracy of Mercury gravity field, Mercury libration, and mean moments of inertia estimations. We did not address the influence of the solar radiation errors, surface albedo errors, and reflectivity errors stemming from spacecraft panel, as these will be investigated in future work.

Cross validation with GEODYN-II indicates the reliability of MERGREAS, and the implementation of the four-way tracking data demonstrates its applicability in Mercury radio science investigations. Such work will provide reference for future Mercury exploration missions; the four-way mode will improve the accuracy of spacecraft orbit, the lander position, the $k_2$, and Mercury gravity field. In our future work, we will simulate satellite-based observations, such as gradiometer, laser altimetry, and navigation images to enhance Mercury spacecraft POD and dynamic parameters recovery, and advance their application in Chinese missions to explore Mercury.

**Acknowledgements** We appreciate Prof. Shuanggen Jin from Shanghai Astronomical Observatory to provide advice in this research. We thank the Mr. Stephen C. McClure, a native English speaker and researcher, and Dr. Yiqun Dai from Wuhan University to help polish this paper. The work is supported by National Scientific Foundation of China (U1831132, 41874010, 41804025) and Innovation Group of Natural Fund of Hubei Province (2018CFA087). This work is also supported by the Open Funding of Astro Dynamic Laboratory (No. 2016ADL-DW0103) and the Open Funding of Macau University of Science and Technology (FDCT 119/2017/A3). JPB is funded by a DAR grant in planetology from the French Space Agency (CNES). The GEODYN-II is authorized by GSFC/NASA and we run it in workstation in Shanghai Astronomical Observatory. The numerical calculations of MERGREAS have been done on the supercomputing system in the Supercomputing Center of Wuhan University.

**Publisher's Note** Springer Nature remains neutral with regard to jurisdictional claims in published maps and institutional affiliations.

## References

Acton, C.H.: Planet. Space Sci. **44**(1), 65–70 (1996)
Acton, C., Bachman, N., Semenov, B., Wright, E.: Planet. Space Sci. **150**, 9 (2017)
Bertone, S., Poncin-Lafitte, C.L., Rosenblatt, P., Lainey, V., Marty, J.C., Angonin, M.C.: Adv. Space Res. **61**(1), 89 (2017)
Böhm, J., Niell, A., Tregoning, P., Schuh, H.: Geophys. Res. Lett. **33**(7) L07304 (2006)
Cicalò, S., Schettino, G., Di, R.S., Alessi, E.M., Tommei, G., Milani, A.: Mon. Not. R. Astron. Soc. **457**(2), 1507 (2016)
Correia, A.C.M., Laskar, J.: Nature **429**, 848 (2004)
Davis, J.L., Herring, T.A., Shapiro, I.I., Rogers, A.E.E., Elgered, G.: Radio Sci. **20**(6), 1593 (1985)
Dumberry, M., Rivoldini, A.: Icarus **248**, 254 (2015)
Ernst, C.M., Murchie, S.L., Barnouin, O.S., Robinson, M.S., Denevi, B.W., Biewett, D.T., Head, J.W., Izenberg, N.R., Solomon, S.C., Roberts, J.H.: Icarus **209**(1), 210 (2010)
ESA Media Relations Office (2018). http://sci.esa.int/jump.cfm?oid=60833
Evans, S., Taber, W., Drain, T., Smith, J., Wu, H.C., Guevara, M., Sunseri, R., Evans, J.: In: 6th International Conference on Astrodynamics Tools and Techniques, Darmstadtium, Germany (2016)
Genova, A., Iess, L., Marabucci, M.: Planet. Space Sci. **81**, 55 (2013)
Genova, A., Goossens, S., Lemoine, F.G., Mazarico, E., Neumann, G.A., Smith, D.E., Zuber, M.T.: Icarus **272**, 228 (2016)
Goossens, S., Matsumoto, K., Rowlands, D.D., Lemoine, F.G., Noda, H., Araki, H.: J. Geod. **85**(8), 487 (2011)
Healy, L.M., Berry, M.M.: A variable-step double-integration multistep integrator. Dissertation Abstracts International 65-02, 0857 (2004)
Iwata, T., Takahashi, M., Namiki, N., Hanada, H., Kawano, N., Heki, K.: J. Geod. Soc. Jpn. **47**(1), 558 (2001)
Johnson, C.L., Hauck, S.A.: J. Geophys. Res. **121**(11), 2349 (2016)
Kaula, W.M.: Theory of Satellite Geodesy: Applications of Satellite to Geodesy. Blaisdell, Waltham (1966)
Khan, A., Liebske, C., Rozel, A., Rivoldini, A., Nimmo, F., Connolly, J.A.D., Plesa, A.-C., Giardini, D.: J. Geophys. Res., Planets **123**, 575–611 (2017)
Lemoine, F.G., Goossens, S., Sabaka, T.J., Nicholas, J.B., Erwan, M., Rowlands, D.D., Loomis, B.D., Chinn, D.S., Caprette, D.S., Neumann, G.A., Smith, D.E., Zuber, M.T.: J. Geophys. Res., Planets **118**(8), 1676 (2013)
Li, F., Ye, M., Yan, J., Hao, W., Barriot, J.P.: Adv. Space Res. **57**(11), 2376 (2016)
Mazarico, E., Genova, A., Goossens, S., Lemoine, F.G., Neumann, G.A., Zuber, M.T., Smith, D.E., Solomon, S.C.: J. Geophys. Res., Planets **119**(12), 2417–2436 (2014)
Montenbruck, O., Gill, E.: Appl. Mech. Rev. **55**(2), 77 (2002)

Moyer, T.D.: Formulation for Observed and Computed Values of Deep Space Network Data Types for Navigation, Monograph 2. Deep Space Communications and Navigations Series. NASA/JPL, Oak Grove (2001)
Moyer, T.D.: Formulation for Observed and Computed Values of Deep Space Network Data Types for Navigation (2005)
Namiki, N., Iwata, T., Matsumoto, K., Hanada, H., Noda, H., Goossens, S., Ogawa, M., Kawano, N., Asari, K., Tsuruta, S., Ishihara, Y., Liu, Q., Kikuchi, F., Ishikawa, T., Sasaki, S., Aoshima, C., Kurosawa, K., Sugita, S., Takano, T.: Science **323**(5916), 900 (2009)
Padovan, S., Margot, J.L., Hauck, S.A. II, Moore, W.B., Solomon, S.C.: J. Geophys. Res., Planets **119**(4), 850 (2014)
Pavlis, D.E., Poulose, S.G., Rowton, S.C., McCarthy, J.J., Luthcke, S.B.: GEODYN operations manuals. Raytheon ITSS contractor report (2000)
Petit, G., Luzum, B.: In: IERS Convention 2010, IERS Technical Note 36. Verlag den Bundesamtes für Kartographie und Geodäsie, Frankfurt (2010)
Potter, A., Morgan, T.: Science **229**(4714), 651 (1985)
Rivoldini, A., Hoolst, T., Verhoeven, O.: Icarus **201**(1), 12 (2009)
Rivoldini, A., Van Hoolst, T.: Earth Planet. Sci. Lett. **377**, 62 (2013)
Saastamoinen, J.: Use Artif. Sat. Geo. 15,247 (1972)
Schettino, G., Tommei, G.: Universe **2**(3), 21 (2016)
Shapiro, I.I.: Phys. Rev. Lett. **13**(26), 789 (1964)
Smith, D.E., Zuber, M.T., Phillips, R.J., Solomon, S.C., Hauck, S.A. II, Lemoine, F.G., Mazarico, E., Neumann, G.A., Peale, S.J., Margot, J.L., Johnson, C.L., Torrence, M.H., Perry, M.E., Rowlands, D.D., Goossens, S., Head, J.W., Taylor, A.H.: Science **336**(6078), 214 (2012)
Stark, A., Oberst, J., Preusker, F., Gwinner, K., Peale, S.J., Margot, J.L.: Planet. Space Sci. **117**(1), 64 (2015)
Takeuchi, H., Saito, M.: Methods Comput. Phys. **11**, 217–295 (1972)
Tapley, B., Schutz, B., Born, G.H.: Radiometric Tracking Techniques for Deep-Space Navigation. Elsevier, Boston (2004)
The state council information office of China (2016). http://www.scio.gov.cn/ztk/dtzt/34102/35723/index.html
Thornton, C.L., Border, J.S.: Radiometric Tracking Techniques for Deep-Space Navigation. Wiley, New York (2003)
Tommei, G., Milani, A., Vokrouhlický, D.: Celest. Mech. Dyn. Astron. **107**(1), 285–298 (2010)
Van Hoolst, T., Jacobs, C.: J. Geophys. Res., Planets **108**(E11) 5121 (2003)
Van Hoolst, T., Sohl, F., Holin, I., Verhoeven, O., Dehant, V., Spohn, T.: Space Sci. Rev. **132**, 203 (2007)
Verma, A.K., Margot, J.L.: J. Geophys. Res., Planets **121**(9) 1627 (2016)
Wieczorek, M.A., Correia, A.C.M., Feuvre, M.L., Laskar, J., Rambaux, N.: Nat. Geosci. **5**(1), 18 (2011)
Williams, J.G., Boggs, D.H., Folkner, W.M.: IOM 335-JW, DB, WF-20130822-106, July 22, Jet Propul. Lab., Pasadena, USA (2013)
Yan, J.G., Yang, X., Ye, M., Li, F., Jin, W.T., Barriot, J.P.: Astrophys. Space Sci. **362**(7), 123 (2017)